Table 1 Ratio of LDI, PCL, and chain extenders and soft segment concentration of SPU and SPUU.

Sample	LDI: PCL: Chain Extender	Chain Extender	Soft Segment Fraction (wt%)
PCL(1250)(100)PDO	4:4:0	PDO	100
PCL(1250)(80)PDO	4:2:2	PDO	80
PCL(1250)(69)PDO	4:1.5:2.5	PDO	69
PCL(1250)(56)PDO	4:1:3	PDO	56
PCL(1250)(0)PDO	4:0:4	PDO	0
PCL(1250)(80)BDA	4:3:1	BDA	80
PCL(1250)(75)BDA	4:2.5:1.5	BDA	75
PCL(1250)(71)BDA	4:2:2	BDA	71
PCL(1250)(64)BDA	4:1.5:2.5	BDA	64
PCL(1250)(53)BDA	4:1:3	BDA	53
PCL(1250)(0)BDA	4:0:4	BDA	0

emission scanning electron microscopy (FE-SEM).

2. EXPERIMENTAL

2.1 Materials

Fig. 1 shows the chemical structures of 2,6-diisocyanatohexanoate (LDI), polycaprolactone diol (PCL), 1,3-propandiol (PDO), and 1,4-butanediamine (BDA). 2,6-Diisocyanatohexanoate (LDI, Kyowa Hakko Co., Ltd.), polycaprolactone diol (PCL, Aldrich Chemical), 1,3-propandiol (PDO, Kanto Chemical. Co., Ltd.), and 1,4-butanediamine (BDA, Aldrich Chemical) were used for the preparation of SPU and SPUU.

LDI, PDO, and BDA were purified by vacuum distillation. PCL was placed in a vacuum oven at 353 K for 24 h to remove residual water before reaction. Dimethylformamide (DMF, Nacalai Tesque, Co., Ltd) was purified by vacuum distillation. Di-*n*-butyltin dilaurate (Tokyo Kasei Kogyo Co., Ltd.) was used as a catalyst for the synthesis of SPU.

2.2 Synthesis of SPU and SPUU

SPU and SPUU were synthesized via a standard two-step prepolymer method and the ratio of soft segment to chain extender was changed.[4] Excess LDI was reacted with PCL. The prepolymer reaction proceeded for 150 min at 358 K. Then the chain extenders (PDO for SPU and BDA for SPUU) was added to the prepolymer and allowed to react for 48 h (SPU) in the presence of 0.1 % of catalyst and for 1 h (SPUU) in DMF. The polymer was then immersed in distilled water for 48 h and dried under vacuum at 353 K for 24 h to remove water.[5] The composition of SPU and SPUU was given in Table 1. Sample names were designated as soft segment (soft segment M_n) (soft segment fraction) chain extender.

All solid films were prepared by solution casting. The SPU and SPUU were dissolved in THF (SPU) and DMF (SPUU). The cast films were dried under vacuum at 393 K for 24 h.

2.3 Characterization of SPU and SPUU

Fourier transform infrared (FT-IR) spectra were obtained with a Spectrum One (Perkin-Elmer. Co., Ltd.) infrared spectrometer. Spectra were generated from 64 scans at 0.5 cm^{-1} resolution. 5 % THF solution of SPU was placed directly onto NaCl and 5 % DMF solution of SPUU were placed directly onto CaF_2. Subsequent evaporation of the DMF at 393 K under vacuum was performed for 24 h.

DSC thermograms from 173 K to 423 K were obtained using a differential scanning calorimeter DSC8230B (Rigaku Denki Co. Ltd.) at a heating rate of 15 K min^{-1} under a dried nitrogen purge. The sample weight was around 8 mg.

Stress-strain measurements were obtained at room temperature using an RTC-1250 (ORIRNTEC. Co., Ltd.). Samples were cut from films cast to 90-120 μm thickness. A cross-head speed of 200 mm min^{-1} was used.

2.4 SPU and SPUU degradation

Degradation studies were performed using tris-buffered saline (TBS, 0.05 M Tris, 0.1M NaCl, pH=7.6).[5] Each samples were placed into an individual vial containing 10 ml TBS, and incubated at 310 K. Samples were removed from buffer following 7, 21, 35, and 70 days. After drying under vacuum for 72 h, samples were reweighed to determine total percentage of mass loss.

2.5 Electrospray Deposition (ES)

For SPU, THF was used as the solvent to prepare the polymer solutions at different concentration for ES. A schematic diagram of the ES device for manufacturing fibers was shown in Fig. 2. The polymer solution was delivered by a programmable pump to the exit hole of the stainless-steel blunt-ended needle electrode (inner diameter; 0.8 mm). An aluminum plate was used as a lower electrode. A positive high DC voltage supply was used to apply the voltage. The flow rate was 1 ml/h. The distance of electrode was 350 mm. The sample solution was electrostatistically drawn from the needle tip and deposited on the lower electrode.

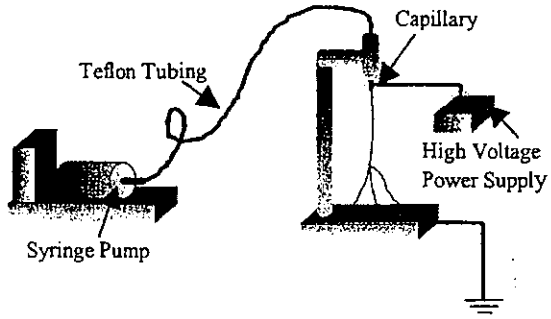

Figure 2 Schematic diagram of the ES apparatus for manufacturing fiber structure.

All the samples were observed with FE-SEM (S-4300SE, Hitachi Co., Ltd.) under the accelerating voltages of 1 kV. The samples were observed without conductive over-coating.

3. RESULTS AND DISCUSSION

3.1 Characterization of SPU and SPUU

Fourier transform infrared (FT-IR) spectroscopy was used to investigate the structural difference in hard and soft segments of SPU and SPUU. IR spectra for the SPU and SPUU are shown in Fig. 3. The absorption bands at 1735 cm^{-1} to 1720 cm^{-1} are associated with the ester carbonyl groups of PCL. The broad shoulders detected at 1670 cm^{-1} to 1710cm^{-1} are assigned to the hydrogen bonded urethane carbonyl group (Fig. 3a). The shoulder from 1620 cm^{-1} to 1680cm^{-1} is ascribed urea carbonyl group (Fig. 3b). The relative intensity of the bands attributed to hydrogen bonded urethane and urea linkage increased with a decrease in hard segment fraction. This result shows that the increase of hydrogen bonding among hard segments with an increase in fraction of chain extender.

The difference in state of molecular aggregation between SPU and SPUU was confirmed by the DSC. The hard segment is amorphous because of the non-symmetric molecular structure of LDI. Fig. 4 shows the DSC thermograms for SPU and SPUU, respectively. A base line shift corresponding to the hard segment glass transition temperature (T_g) was observed in the 308 K in SPU (Fig. 4a). It seems that the non-symmetric diisocyanate (LDI) produces hard segment that was unable to pack efficiently. However, the hard segment T_g was observed 379 K in DSC curves of SPUU. This is because the urea linkage has strong hydrogen bonding compared with that of the urethane linkage. Soft segment crystal melting was observed in the range of 283 K to 320 K (Fig.4a). Crystallinity of SPU decreased

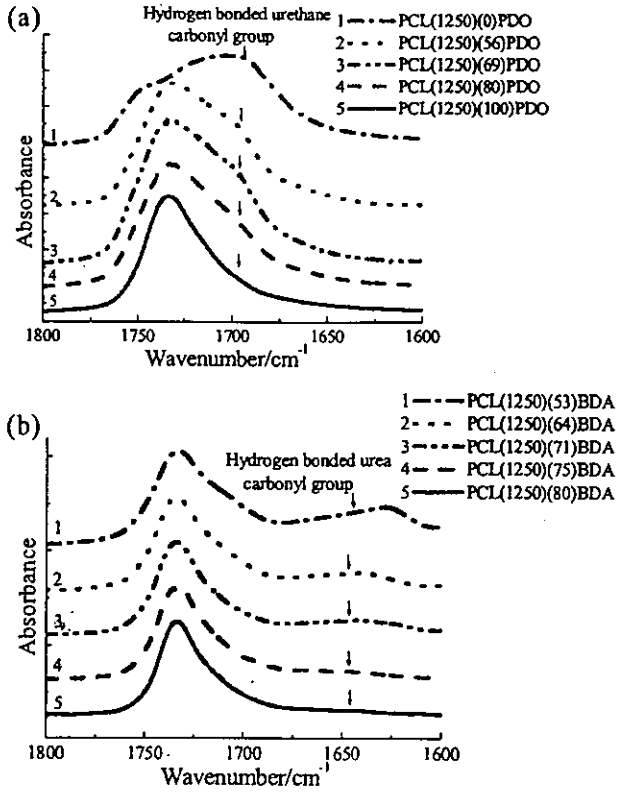

Figure 3 FT-IR absorbance spectra of (a) SPU series and (b) SPUU series.

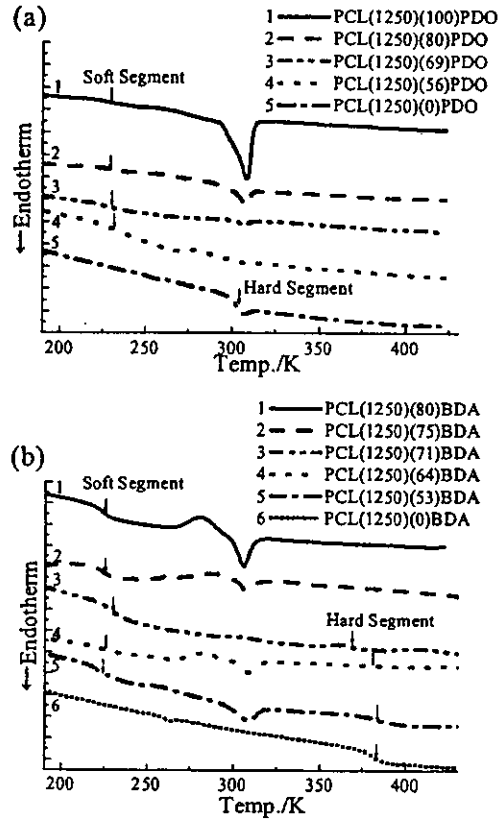

Figure 4 DSC scans of (a) SPU series and (b) SPUU series.

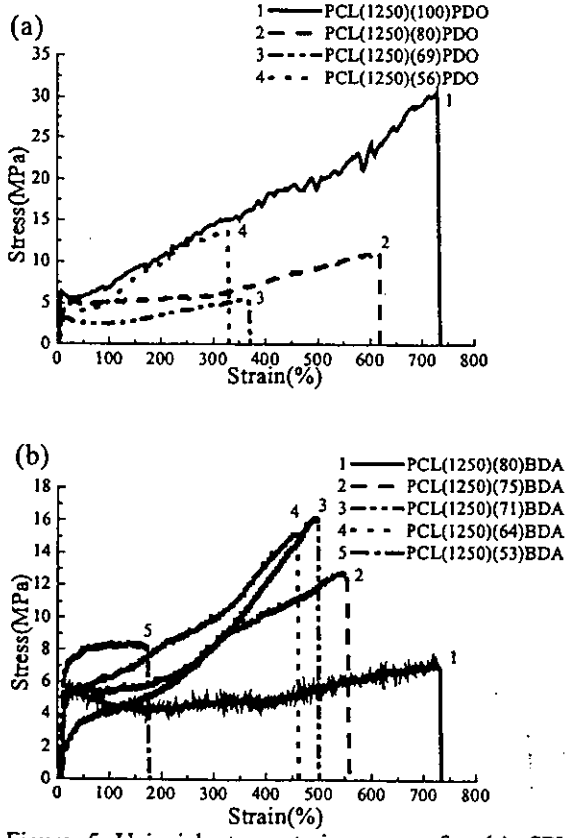

Figure 5 Uniaxial stress-strain curves for (a) SPU series and (b) SPUU series.

with a decrease in PCL fraction. This is due to the partial solubilization of hard segment into PCL phase. PCL(1250)(71)BDA showed higher soft segment T_g than other SPUU's (Fig. 4b). These shifts of T_g are attributed to the partial solubilization of hard segment into PCL phase. Phase separation proceeded with the increase of hard segment because of strong hydrogen bonding.

3.2 Mechanical properties of SPU and SPUU

The mechanical properties of SPU and SPUU were investigated by stress-strain measurement. Typical stress-strain curves for SPU and SPUU are shown in Fig. 5. The results suggested that the increasing modulus and decreasing the ultimate strain with increasing the hard segment fraction of SPU (Fig. 5a). This result showed that the PCL crystallites may act as physical cross-links. In contrast, PCL(1250)(71)BDA showed the excellent elastic properties (Fig. 5b). This is because the BDA formed strong aggregated hard segment and the loss of crystallinity of PCL soft segment.

3.3 Degradation of SPU

The degradation characteristics of a series of SPU were evaluated. The mass loss data for SPU samples were shown in Fig 6. The magnitude of degradation in SPU was increased with an increase in the soft segment fraction. This is because the soft segment has the hydrolyzable ester linkages and is susceptible to hydrolysis compared with that of the urethane linkage.

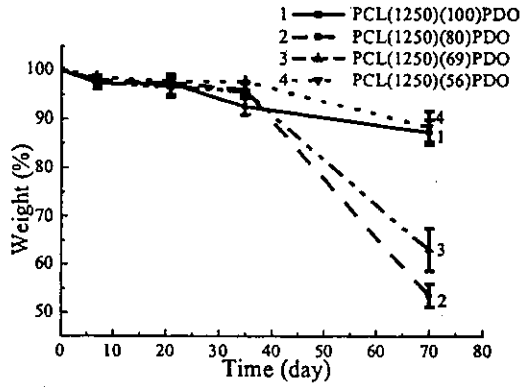

Figure 6 Degradation behavior of SPU in pH=7.6 at 310 K.

3.4 Electrospray deposition (ES)

In ES experiment, morphological change of the deposited ES microstructure is expected when the concentration of polymer solutions were changed. Fig. 7 showed FE-SEM images of SPU. FE-SEM images showed that a mixture of large beads and fibers were formed by ES at 20 wt% PCL(1250)(80)PDO solution under voltage of 13.5 kV (Fig. 7a). In contrast, fine fibers was formed at 30 wt% PCL(1250)(80)PDO solution under voltage of 15.4 kV (Fig. 7b). It was shown that higher concentration of solution favored to form of uniform fibers without beads-like structure. This is because the critical viscosity in solution needs to be exceeded in order to fabricate fibers.[6] Below this viscosity chain entanglement are insufficient to stabilize the jet, leading to spraying of droplets.

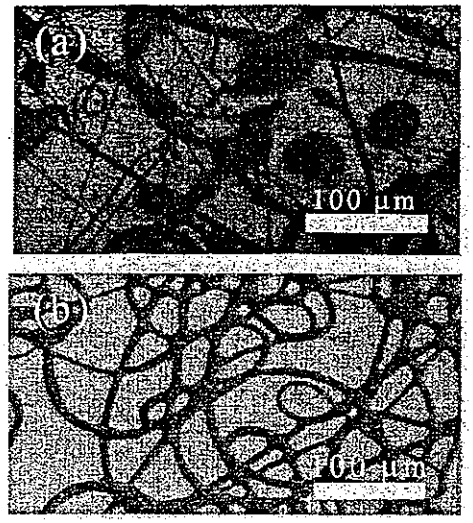

Figure 7 FE-SEM images of microstructure of electrospray deposited PCL(1250)(80)PDO. (a) 20 wt% under voltage of 13.5 kV and (b) 30 wt% under voltage of 15.4 kV.

4. CONCLUSION

Biodegradable segmented polyurethanes (SPU) and segmented poly(urethaneurea)s (SPUU) derived from a lysine-based diisocyanate were synthesized and characterized. IR spectroscopy revealed that the increase of hydrogen bonding among the hard segment with an increase in chain extender fraction. DSC thermogram revealed that the BDA-based hard segment T_g is higher than that of PDO-based one. Tensile tests revealed the excellent elastic properties of PCL(1250)(71)BDA. The magnitude of degradation of SPU was increased with an increase in the soft segment fraction. ES technique was used to fabricate biodegradable fibers. It was shown that higher concentration of solution favored to form of uniform biodegradable micro-fibers without beads-like structure.

Acknowledgement

This work was supported by a Grant-in-Aid for Scientific Research from Ministry of Health, Labor and Welfare (MHLW) of Japan and P&P, Green Chemistry, of Kyushu University.

References

[1] K. A. Athanasiou, G. G. Niederauer and C. M. Agrawal, *Biomaterials.*, **17**, 93(1996).
[2] P. Bruin, G. J. Veenstra, A. J. Nijenhuis, A. J. Pennings, *Makromol Chem Rapid Commun.*, **9**, 589(1988).
[3] J. M. Deitzel, J. Kleinmeyer, D. Harris, N. C. Beck Tan, *Polymer*, **42**, 261(2001).
[4] D. J. Lyman, *J.Polym.Sci.*, **45**, 49(1960).
[5] G. A. Skarja and K. A. Woodhouse, *J. Biomater. Sci. Polymer Edn*, **13**, 391(2002).
[6] E. Kenawy, J. M. Layman, J. R. Watkins, G. L. Bowlin, J. A. Matthews, D. G. Simpson, G. E. Wnek, *Biomaterials*, **24**, 907(2003).

(Received October 11, 2003; Accepted August 31, 2004)

Macromolecular Symposia in press

Charcterization of Novel Bio-degradable Segmented Polyurethanes Prepared from Amino-acid Based Diisocyanate

Atsushi Takahara[1,2], Michiko Hadano[1], Tomohiro Yamaguchi[1], Hideyuki Otsuka[1,2], Satoru Kidoaki[3], Takehisa Matsuda[3]*

[1]Graduate School of Engineering, [2]Institute for Materials Chemistry and Engineering, Kyushu University, Hakozaki, Higashi-ku, Fukuoka 812-8581, JAPAN e-mail: takahara@cstf.kyushu-u.ac.jp
[3]Graduate School of Medicine, Kyushu University, Maidashi, Higashi-ku, Fukuoka 812-8582, JAPAN

Summary: Segmented polyurethanes (SPUs) which were expected to yield non-toxic degradation products were synthesized from lysine-based diisocyanate (LDI), 1,3-propanediol (PDO), and polycaprolactone diol (PCL). SPUs were synthesized via a standard two-step prepolymer method. The hard segment fraction was changed in order to tune the mechanical properties and the degradability. The aggregation structures of the SPUs were characterized by infrared spectroscopy and differential scanning calorimetry(DSC), temperature dependence of dynamic viscoelasticity, and small-angle X-ray scattering(SAXS). DSC and dynamic viscoelastic measurements revealed that the glass transition temperature (T_g) of soft segment increased with an increase in hard segment fraction. SAXS of SPUs revealed the aggregation states of hard and soft segments. Furthermore, the degradation of SPUs was investigated by exposing the polymers to buffer solution at 310 K (pH=7.6). The degradation rate of SPUs increased with an increase in soft segment fraction. This is because the soft segment has the hydrolyzable ester linkages and the ester linkages are susceptible to hydrolysis compared with the urethane linkages. Finally, an electrospray deposition method was used to fabricate biodegradable SPU micro-fibers. FE-SEM images showed that higher concentration of solution favored to form uniform biodegradable micro-fibers without beads-like structure.

Keywords: Segmented polyurethane; lysine-based diisocyanate; biodegradation; microfiber, electro-spray deposition

Introduction

A variety of biodegradable polymers have been developed in the last two decades. However, the majority of these polymers are typically hard and brittle plastics and few biodegradable

elastomeric polymers have been synthesized so far [1-3]. The recent development of diisocyanates based on lysine has removed an obstacle to synthesize biodegradable segmented polyurethane (SPU) elastomers expected to yield non-toxic degradation products [4]. If the lysine-based diisocyanate component in SPU was liberated by hydrolysis of the urethane bonds of the polymer during degradation, the product would be a lysine derivative, an essentially non-toxic product.

In this study, the segmented polyeurethanes (SPUs) were synthesized from lysine-based

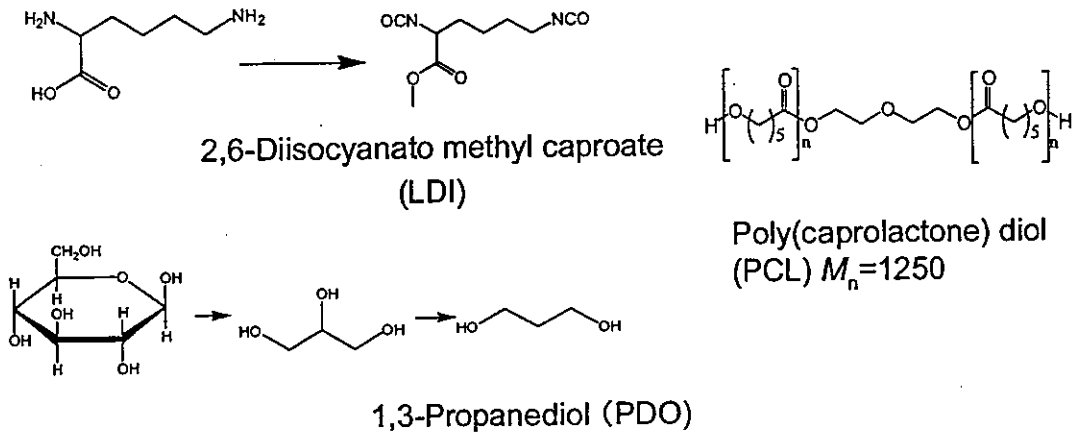

Figure 1 Chemical structures of components of SPU. LDI and PDO can be synthesized from lysine and glucose, respectively.

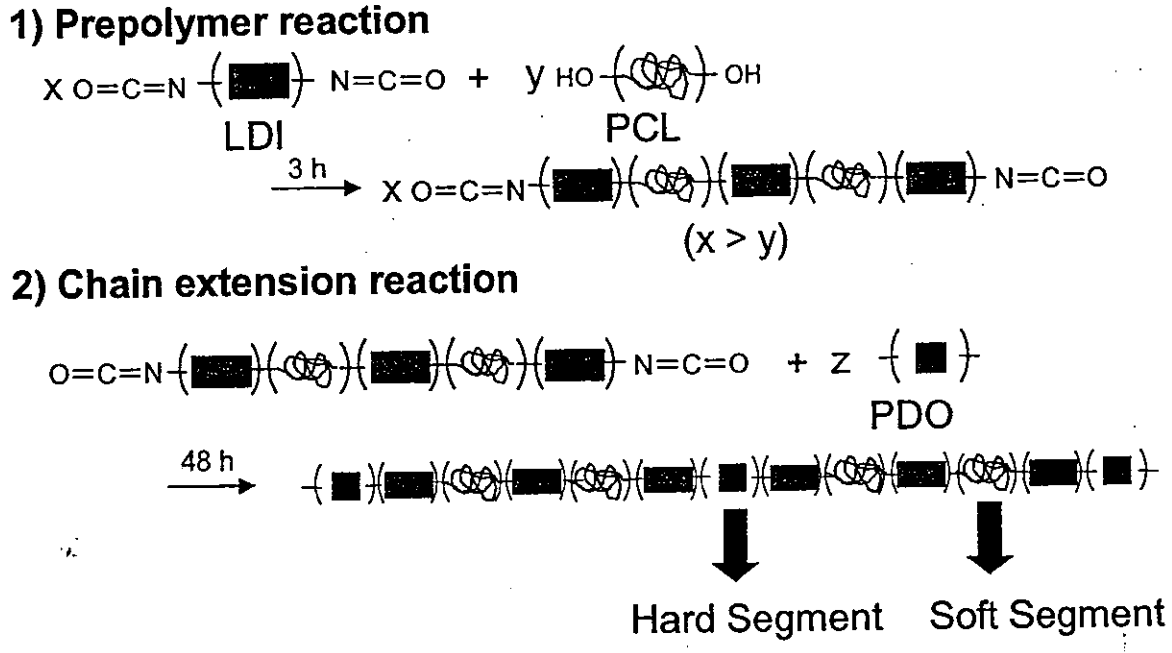

Figure 2 Schematic representation of synthesis of segmented polyurethane(SPU).

diisocyanate. The physical and structural characterizations of SPU were performed. The degradation behavior of SPUs was also investigated. Finally, in order to discuss the possibility of the design of tissue-engineering scaffold, electro-spray deposition (ESD) technique was used to fabricate biodegradable microfibers and microfiber mesh.

Experimental

Materials. 2,6-Diisocyanatohexanoate (LDI), polycaprolactone diol (PCL), and 1,3-propandiol (PDO) were used for the preparation of SPU. PCL with M_n of 1250 was obtained from Aldrich Chemical (Milwaukee, WI, U.S.A.). PCL was placed in a vacuum oven at 333 K to remove residual water before reaction. PDO and LDI were obtained from Kanto Chemical Co. (Tokyo, Japan) and Kyowa Hakko Kogyo Co. (Tokyo, Japan), respectively, and they were distilled under vacuum before use. Their chemical structures were summarized in Figure 1.

Synthesis of Segmented Polyurethanes. SPUs were synthesized via a standard two-step prepolymer method [5,6,7] and the ratio of soft segment to chain extender was changed in order to control the mechanical properties and degradation behavior. Figure 2 shows schematic representation of synthesis of segmented polyurethane(SPU). Excess LDI was reacted with PCL as prepolymer reaction for 150 min at 358 K. Then, the PDO chain extender was added to the prepolymer and allowed to react for 48 h in the presence of dibutyltin dilaurate (0.1 mol%) as a catalyst in *N,N*-dimethylformamide (DMF). The resulted polymer was precipitated by slowly pouring solution into water and the obtained polymer powder was washed with methanol and water. Then, the polymer was dried under vacuum at 353 K for 24 h to remove water. The obtained polymers were multi-block copolymers of hard and soft segments. Soft segment consists of PCL and LDI, whereas hard segment consists of LDI and PDO. Gel permeation chromatography (GPC) was used to determine the molecular weight of SPU. M_w of SPU was in the range of 53k to 86k with M_w/M_n of ca.1.75. Samples were designated as "PCL (M_n of PCL) (PCL fraction) PDO". All solid films were prepared by solution casting from THF solution. The cast films were dried under vacuum at 393 K for 24 h.

Characterization. SPU films were characterized by dynamic viscoelastic measurement, small-angle X-ray scattering (SAXS), Fourier transform infrared (FT-IR) spectroscopy, differential scanning calorimetry (DSC), and tensile tests.

Degradation Behavior. Degradation studies were performed using tris-buffered saline (TBS, 0.05 M Tris, 0.1M NaCl, pH=7.6). Each SPU film with 10 mm x10 mm x 0.9 mm in dimension was placed into an individual vial containing 10 ml TBS, and incubated at 310 K.

Samples were removed from buffer following 7, 21, 35, and 70 days. After drying under vacuum for 72 h, samples were reweighed to determine total percentage of weight loss.

Electro-spray Deposition. Chloroform was used as the solvent to prepare the polymer solutions at different concentration for ESD. The details of ESD equipment was reported elsewhere [8]. The polymer solution was delivered by a programmable pump to the exit hole of the electrode. A positive high-voltage supply was used to supply the voltage. The flow rate was 1 ml h^{-1} and the distance of electrode was 300 mm. The electrosprayed mesh was prepared on to the substrate through continuous deposition with transverse movement of substrate. All the samples were observed with FE-SEM (Hitachi, S-4300) under the accelerating voltages of 1 kV without conductive over-coating.

Results and discussion

Characterization. FT-IR spectroscopy was used to investigate the structural difference in hard and soft segments of SPUs with various PCL fractions. Figure 3 shows the IR spectra of SPUs. The broad shoulders detected at 1730-1750 and 1680-1710cm^{-1} are assigned to the free and hydrogen-bonded urethane and ester carbonyl groups, respectively. The relative intensity of the bands attributed to hydrogen-bonded carbonyl groups increased with an increase in hard segment fraction. This result suggests that hydrogen bonding of carbonyl groups increases with an increase in fraction of PDO chain extender.

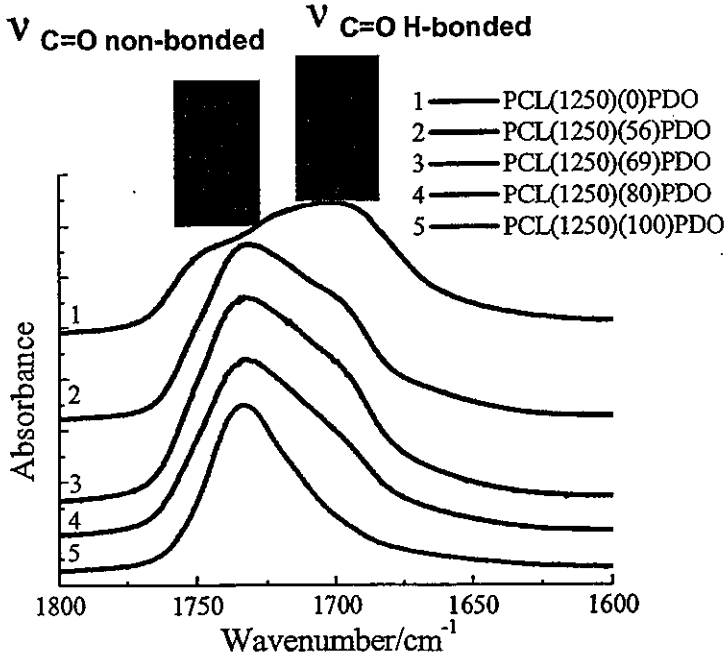

Figure 3 Transmission IR spectra of SPU in the carbonyl stretching region

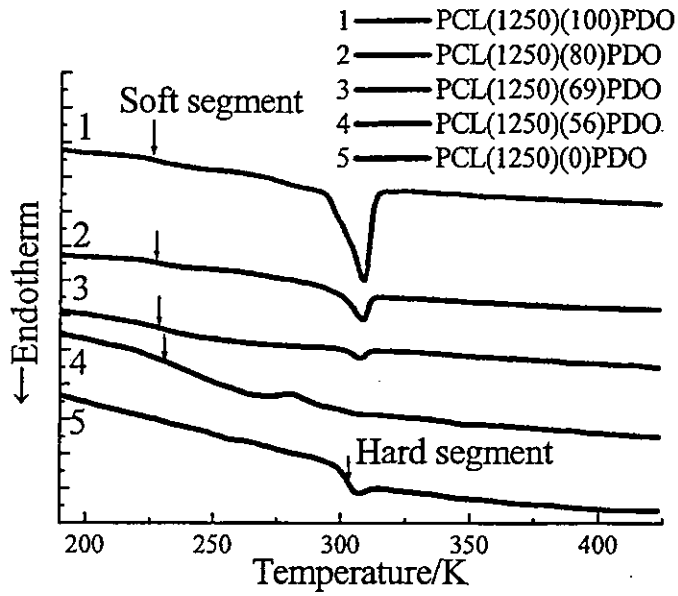

Figure 4 DSC thermograms for SPU with various soft segment contents.

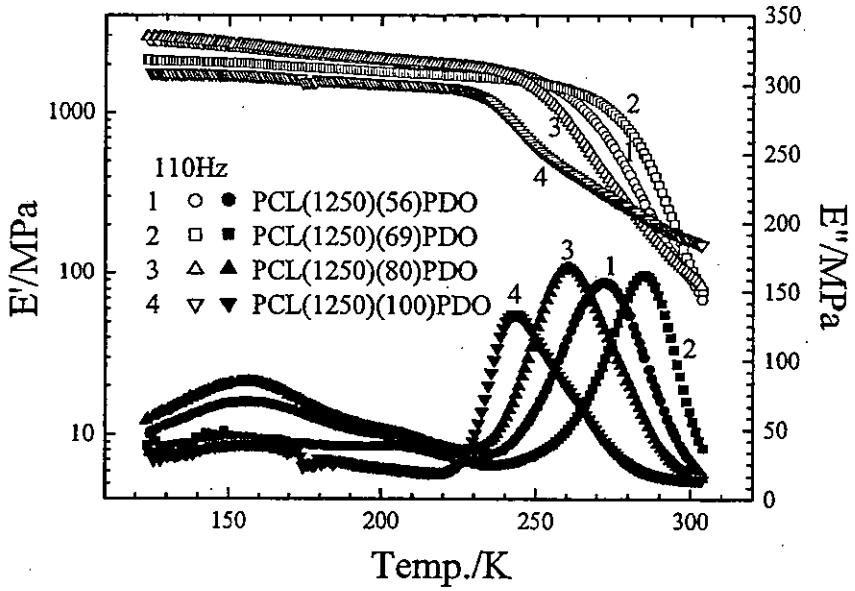

Figure 5 Temperature dependence of dynamic storage modulus, E' and dynamic loss modulus, E" for SPU with various soft segment content.

The difference in state of molecular aggregation of SPUs was confirmed by DSC. Figure 4 shows DSC thermograms for SPU with various soft segment contents. A base line shift corresponding to the hard segment T_g was observed at 302 K. It seems that the non-symmetric diisocyanate (LDI) produces hard segments that were unable to pack efficiently to form crystalline hard segment domain. This also gives the low T_g of hard segment compared with that of aromatic diisocyanate-based hard segment. T_g and crystal melting of PCL in soft segment were observed in the ranges of 225 K to 235 K and 283 K to 320 K, respectively. Crystallinity of PCL in SPUs decreased with a decrease in PCL fraction. This is because of the partial solubilization of hard segment in PCL phase.

The state of thermal molecular motion of SPUs was characterized by dynamic viscoelastic measurement. Temperature dependence of dynamic viscoelasticity was measured at 110Hz from 130 to 310 K under dried nitrogen purge. Figure 5 shows the temperature dependence of dynamic storage modulus, E' and dynamic loss modulus, E" for SPUs with various soft segment contents. A large decrease in E' was observed due to the onset of micro-Brownian motion of PCL soft segment following by the melting of PCL crystallite. Since more than two relaxations were overlapped at around 300 K, it is difficult to separate the relaxation mechanisms at this temperature region. Since the hard segment T_g and melting temperature of PCL were located at ca.300 K, a constant modulus at rubbery plateau was not observed for SPU at above room temperature. Since PCL(1250)(100)PDO does not have low T_g hard segment, a crossover of E' was observed at 280-300K. A broad peak observed at ca.150 K is assignable to γ-absorption of PCL soft segment.

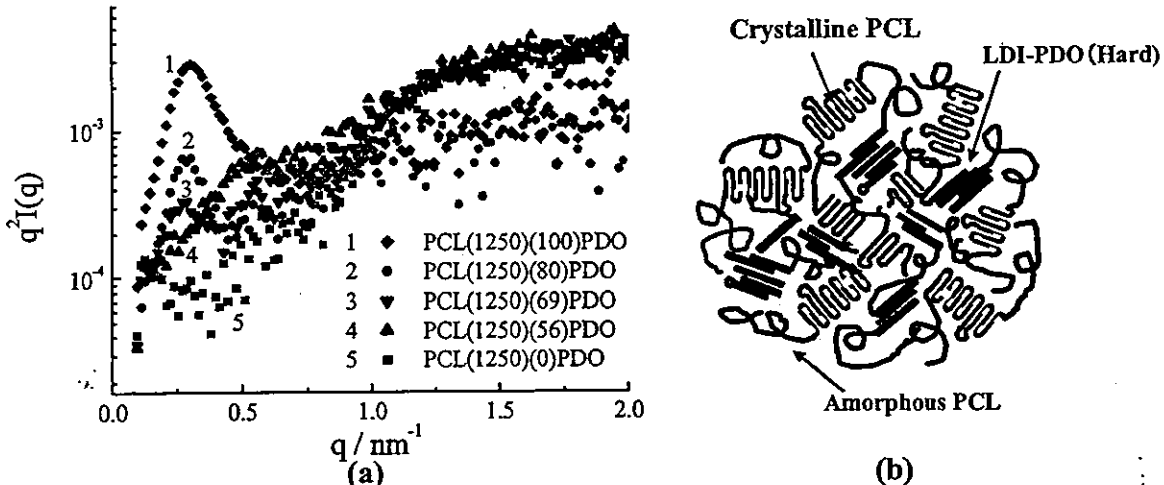

Figure 6 (a) Dependence of corrected intensity on scattering vector for PCL(1250)(X)PDO and (b) structure model of PCL(1250)(X)PDO.

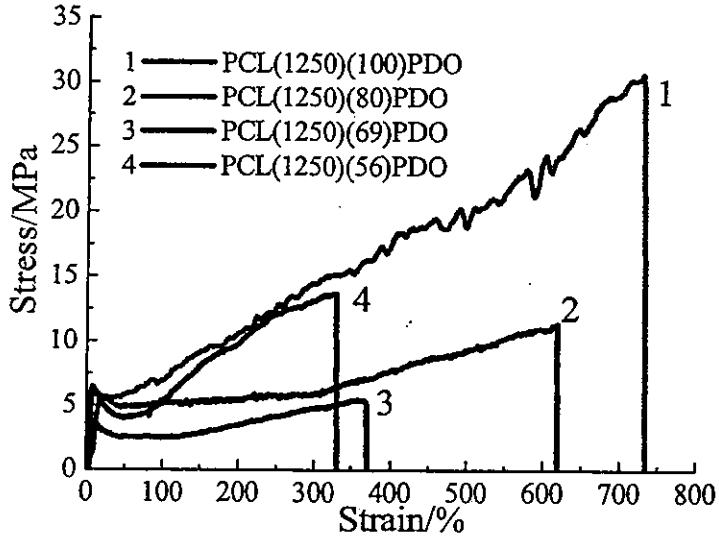

Figure 7 Stress-strain curves for SPU with various soft segment fraction.

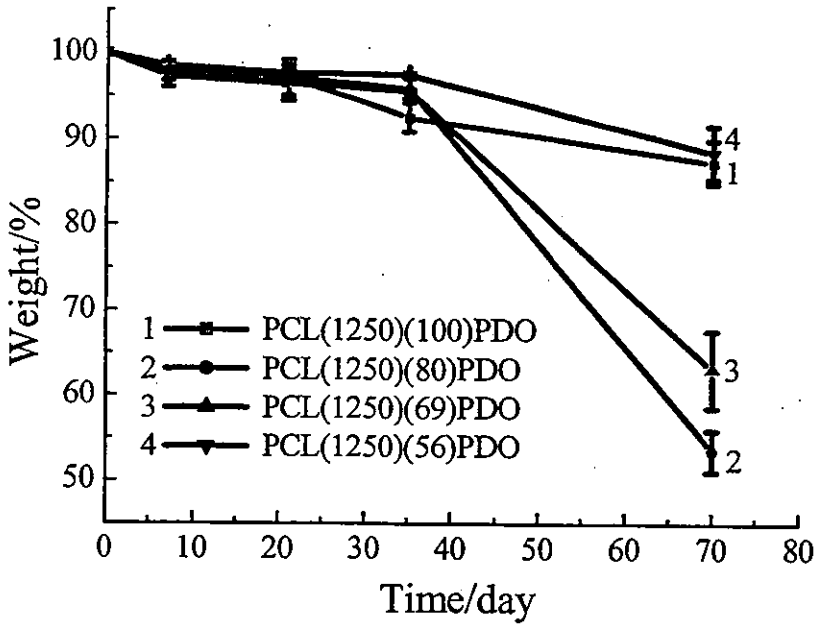

Figure 8 The change in weight with time after immersion in Tris-buffer solution at 310K for SPUs with various soft segment contents.

The phase structure of SPUs was characterized by synchrotron SAXS. SAXS was measured at BL10C at Photon Factory, KEK, Tsukuba, Japan. Figure 6 (a) shows the dependence of corrected intensity on scattering vector of PCL(1250)(X)PDO. q is defined as $4\pi\sin\theta/\lambda$, where θ and λ are Bragg angle and wavelength of X-ray, respectively. Lorentzian factor was corrected by multiplying q^2 to the intensity. A large peak observed at q=ca.0.27 nm^{-1} is attributed to the long period between PCL crystallite. Even the PCL(1250)(100)PDO without hard segment component, the long period was clearly observed. The intensity of this peak decreased with an increase in hard segment fraction and finally disappeared for the LDI-PDO homopolymer. The scattering peak corresponding to the distance between hard segment domains was not observed in SPUs. This can be explained either by the partial phase mixing of hard and soft segments or the absence of the difference in electron density between hard and soft segments. The structure model of PCL(1250)(X)PDO based on above mentioned characterization is depicted in Figure 4(b). PCL formed folded lamellar crystal between hard segment domains. Fairy large amount of amorphous PCL might be present in the soft segment phase. Since the PCL form the large crystallite, PCL(1250)(X)PDO forms three phase structure consists of glassy hard segment, amorphous PCL and crystalline PCL phase.

The mechanical properties of SPUs were investigated by stress-strain measurement. Figure 7 shows the stress-strain curves for SPUs with various PCL fractions. Below T_g of hard segment (302K) and T_m of PCL(283-320K), both hard segment and crystalline PCL phase can act as crosslink at low elongation. However, the PCL crystallite is easily deformed at this temperature, the yielding was observed at low elongation region. Beyond the yielding point, the amorphous PCL phase with low T_g act as rubber elastic component. On the other hand, the elongation at break increased with an increase in soft segment fraction.

Degradation Behavior. The degradation characteristics of a series of SPUs were evaluated. Figure 8 shows the change in weight with time after immersion in Tris-buffer solution at 310 K for SPUs with various soft segment contents. At 310 K, PCL phase in SPU might be melted and the hard segment is in leather like state. The magnitude of degradation in SPUs was increased with an increase in the soft segment fraction. This is because the soft segment has the hydrolyzable ester linkages and the ester linkages are susceptible to hydrolysis compared with the urethane linkages. On the other hand, PCL-LDI soft segment homopolymer showed small magnitude of degradation. This can be ascribed to the presence of PCL crystallites at 310 K.

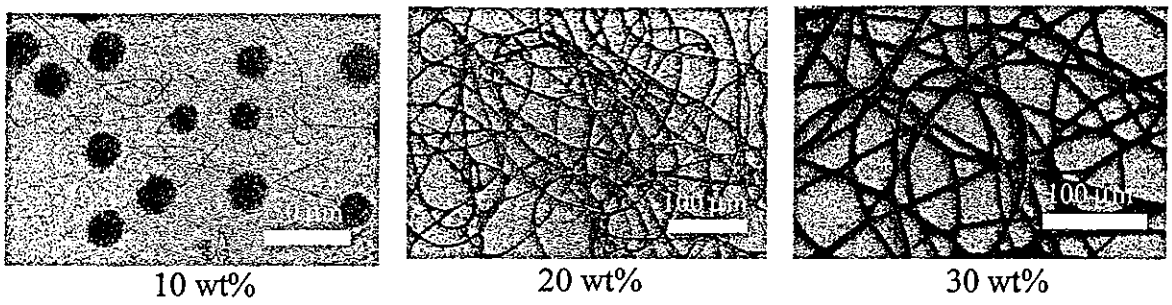

Figure 9 FE-SEM images of microstructure of PCL(1250)(80)PDO ESD microfibers prepared at 10-30 wt% chloroform solution under voltage of 12 kV.

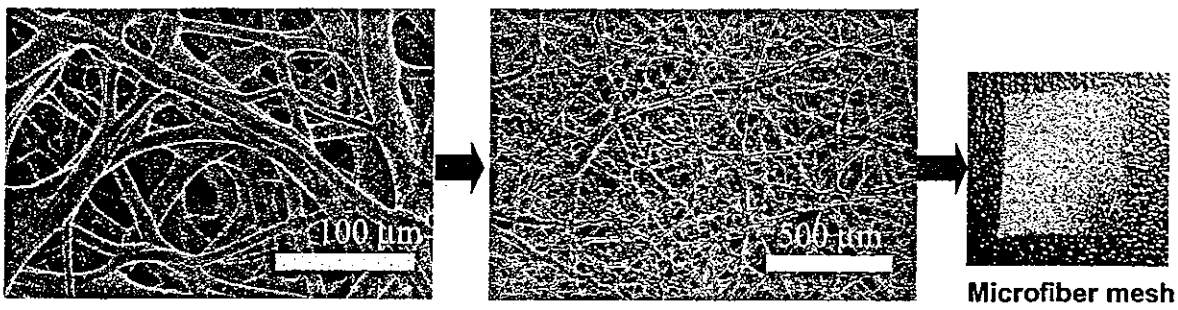

Figure 10 FE-SEM images of SPU microfiber mesh prepared by ESD.

Electro-spray Deposition. In ESD experiment, morphological change of the electrospray deposited microstructure is expected when the concentration of polymer solutions was changed. Figure 9 shows FE-SEM images of PCL(1250)(80)PDO ESD microfibers deposited from 10-30wt% solution under 12 kV. FE-SEM images showed that a mixture of large beads and fibers were formed by ESD at 10 wt% PCL(1250)(80)PDO solution under voltage of 12 kV. In contrast, fine fibers were formed at 20 wt% and 30wt% PCL(1250)(80)PDO solution. The average diameters of the fibers prepared at 10wt%, 20wt%, and 30wt% were 1.0 μm, 7.5 μm, and 7.7 μm, respectively. It was shown that higher concentration of solution favored to form uniform fibers without beads-like structure. This is because the critical viscosity in solution needs to be exceeded in order to fabricate fibers. Below this viscosity chain entanglements are insufficient to stabilize the jet, leading to spraying of droplets. A repeated deposition of microfiber with transverse movement of substrate gives mesh of SPU microfibers. Figure 10 shows FE-SEM images of PCL(1250)(80)PDO microfiber mesh prepared from 35 wt% solution under 12 kV with flow rate of 1 ml h^{-1}. The average diameters

of the fibers was 11.6 μm As shown in Figure 10, self-standing microfiber mesh with high porosity was successfully obtained from ESD of SPU.

Conclusion

Novel biodegradable segmented polyurethanes were prepared from lysine-based diisocyanate, PCL, and PDO chain extender. DSC, dynamic viscoelastic measurements, and small-angle X-ray scattering experiment revealed that the SPU has amorphous PCL, crystalline PCL, and glassy hard segment structure. Degradation rate of SPUs was confirmed by the exposure of SPU film to buffer solution. Microfibers and microfiber mesh of SPU were successfully prepared by electro-spray deposition.

Acknowledgement

This work was partially supported by a Grant-in-Aid for Scientific Research from Ministry of Health, Labor and Welfare (MHLW) of Japan, a Grant-in-Aid for Scientific Research (A)(2) (No.15205028) from Japan Society for the Promotion of Science and P&P, Green Chemistry, of Kyushu University. The SEM observation was made using FE-SEM at the Kyushu University Station-II for collaborative research.

References

[1] K. A. Athanasiou, G. G. Niederauer and C. M. Agrawal, *Biomaterials*, **17**, 93(1996).

[2] P. Bruin, G. J. Veenstra, A. J. Nijenhuis, A. J. Pennings, *Makromol. Chem. Rapid Commun.*, **9**, 589(1988).

[3] J. M. Deitzel, J. Kleinmeyer, D. Harris, N. C. Beck Tan, *Polymer*, **42**, 261(2001).

[4] G. A. Skarja and K. A. Woodhouse, *J. Biomater. Sci. Polymer Edn.*, **13**, 391(2002).

[5] D. J. Lyman, *J. Polym. Sci.*, **45**, 49(1960).

[6] A. Takahara, J. Tashita, T. Kajiyama, M. Takayanagi, W. J. MacKnight, *Polymer*, **26**, 987(1985).

[7] A. Takahara, K. Takahash, T. Kajiyama, *J. Biomater. Sci., Polym. Ed.*,**5**, 183 (1993).

[8] S. Kidoaki, I.K. Kwon, T. Matsuda, *Biomaterials*, **26**, 37(2005).

ELSEVIER

Journal of Orthopaedic Research 22 (2004) 104–109

Journal of Orthopaedic Research

www.elsevier.com/locate/orthres

Anatomical analysis of the femoral condyle in normal and osteoarthritic knees

Shuichi Matsuda [a,*], Hiromasa Miura [a], Ryuji Nagamine [a], Taro Mawatari [a], Masami Tokunaga [b], Ryotaro Nabeyama [a], Yukihide Iwamoto [a]

[a] *Department of Orthopaedic Surgery, Graduate School of Medical Sciences, Kyushu University, 3-1-1 Maidashi, Higashi-Ku, Fukuoka City, Fukuoka 812-8582, Japan*

[b] *Fukuoka Orthopaedic Hospital, 2-10-50 Yanagouchi, Minami-Ku, Fukuoka city, Fukuoka 815-0063, Japan*

Accepted 21 May 2003

Abstract

It is important to understand anatomical feature of the distal femoral condyle for treatment of osteoarthritic knees. Detailed measurement of the femoral condyle geometry, however, has not been available in osteoarthritic knees including valgus deformity. This study evaluated femoral condyle geometry in 30 normal knees, 30 osteoarthritic knees with varus deformity, and 30 osteoarthritic knees with valgus deformity using radiographs and magnetic resonance imaging (MRI). In radiographic analysis in the coronal plane, the femoral joint angle (lateral angle between the femoral anatomic axis and a tangent to femoral condyles) was 83.3° in the normal knees, 83.8° in the varus knees, and 80.7° in the valgus knees. In MRI analysis in the axial plane, the posterior condylar tangent showed 6.4° of internal rotation relative to the transepicondylar axis in the normal knees, 6.1° in the varus knees, and 11.5° in the valgus knees. These results suggested that there was no hypoplasia of the medial condyle in the varus knees, but the lateral condyle in the valgus knees was severely distorted. Surgeons should take this deformity of the lateral femoral condyle into account when total knee arthroplasty is performed for a valgus knee.

Keywords: Knee; Osteoarthritis; Surface geometry; Magnetic resonance imaging

Introduction

Correct rotational alignment of the femoral component is essential for achieving proper varus and valgus stability and patellar tracking in total knee arthroplasty. Anatomical and biomechanical studies have shown that the transepicondylar axis is a reliable rotational landmark [7,10–12,23]. The anteroposterior (AP) axis, which is approximately perpendicular to the epicondylar axis, is used as a rotational landmark for the femoral component [3]. On the other hand, posterior condyles are also used as a rotational landmark when total knee arthroplasty is performed, because the posterior condyles can be more easily identified intraoperatively than the transepicondylar axis.

Current cutting guides for the distal femur allow externally rotation of the femoral component a few degrees relative to the posterior condyles. However, the anatomical features of the posterior condyles vary with deformity, and the use of the fixed externally rotated angle for all knees can result in rotational malalignment of the femoral component. Varus knees do not demonstrate hypoplasia or severe wear of the posterior part of the medial condyle [13], but the lateral femoral condyle may appear hypoplastic in valgus knees [16,20]. Detailed geometric measurements of the distal femur, however, have not been available in osteoarthritic knees with valgus deformity. This study evaluated the surface geometry in normal, varus, and valgus knees using magnetic resonance (MRI) imaging and radiographs to determine whether hypoplasia of the lateral condyle exists in the valgus knee.

Methods

The subjects gave informed consent and an institutional review board approved the study. Thirty normal knees in 27 healthy volunteers, 30 osteoarthritic knees with varus deformity in 30 patients and

* Corresponding author. Tel.: +81-92-642-5447; fax: +81-92-642-5507.

E-mail address: mazda@ortho.med.kyushu-u.ac.jp (S. Matsuda).

0736-0266/$ - see front matter © 2003 Orthopaedic Research Society. Published by Elsevier Ltd. All rights reserved.
doi:10.1016/S0736-0266(03)00134-7

Table 1
Clinical data for each group

Parameter	Normal knees	Varus knees	Valgus knees
Age	66.2 ± 6.5	67.9 ± 5.0	71.5 ± 11.3
Gender			
Male	10	8	2
Female	20	22	28
Knee society score	100.0 ± 0.0	49.3 ± 16.9	54.4 ± 18.8

30 osteoarthritic knees with valgus deformity in 26 patients were evaluated using MRI (Table 1). Subjects with the normal knees had no knee symptoms, and no osteoarthritic changes were detected on plain radiographs. Physical examination showed no abnormal findings. Patients with the varus and valgus knees had signs and symptoms of osteoarthritis. Standing radiographs showed the complete loss of the medial joint space in the varus knees, and of the lateral joint space in the valgus knees. Based on the case history, physical examination, and laboratory tests, patients with rheumatoid arthritis and other inflammatory diseases or metabolic conditions were excluded from the study. No subject had a history of injury to the knees.

MRI analysis

MRI was performed using a 0.5 T whole body MR imaging system (MRP-5000AD, Hitachi Medical Corp, Kashima, Japan) with an extremity coil, and all the subjects were restrained from moving during the scanning process. Pulse sequences were T1-weighted images (500/20, TR/TE). The direction of axial slice imaging placed the slice perpendicular to the femoral mechanical axis in the coronal plane and perpendicular to the long axis of the femur in the sagittal plane. The axial slice on the most prominent part of both femoral condyles was selected for analysis.

The transepicondylar axis was defined as a line between the most medial and the most lateral prominences of the epicondyles, and the posterior condylar tangent as a line connecting the posterior aspects of the femoral condyles [3,13] (Fig. 1). Articular boundaries of the femoral condyles were used for posterior condylar tangent. The AP axis was a line connecting the deepest part of the patellar groove anteriorly and the mid point between the most posterior part of the condyle [3]

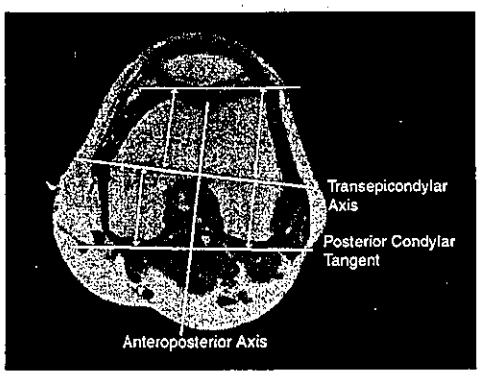

Fig. 1. Magnetic resonance image of the axial view of the distal femur. A line was drawn perpendicular to the transepicondylar axis from the most anterior part of each anteorior condyle. The distance (a) was defined as AP dimension of the anterior part of the medial femoral condyle and the distance (b) was defined as that of the lateral femoral condyle. A line was drawn perpendicular to the transepicondylar axis from the most posterior part of each posterior condyle. The distance (c) was defined as the AP dimension of the posterior part of the medial femoral condyle and the distance (d) was defined that of the lateral femoral condyle.

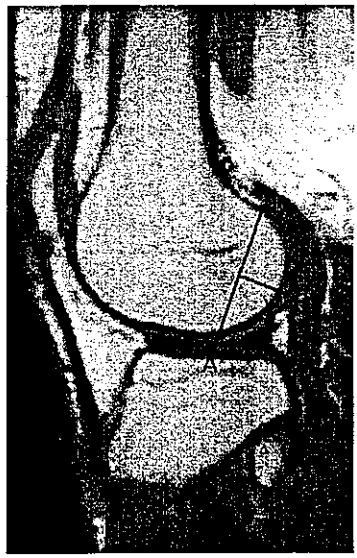

Fig. 2. Magnetic resonance image of the sagittal view of the distal femur. A line (Line A–B) was drawn from the most distal point on the surface articulating with the tibia (A) to the most superior point of the femoral articular surface of the posterior condyle (B). Another line was drawn perpendicular to Line A–B from its midpoint to the femoral articular surface. The point where this line met the femoral articular surface was defined as point C. The arc A–B was defined as the posterior part of the femoral condyle, and point A, B, and C were used for calculation of the radius in the posterior part of the condyle.

(Fig. 1). The angle between the transepicondylar axis and the posterior condylar tangent and the angle between the line perpendicular to the AP axis and the posterior condylar tangent were measured and compared among the normal, varus and valgus knees. The lateral angle between the transepicondylar axis and the AP axis was also measured in each group. The AP dimensions of both the medial and lateral condyles were measured (Fig. 1).

Sagittal plane sections through the most prominent part of both femoral condyles were used for measurement. The articular surface of each condyle was divided into distal and posterior parts (Fig. 2). The posterior part was assumed to fit a circular arc [7,13], and the radius of the arc was calculated using three points on the articular surface of each part. The radius was calculated using:

$$R = \frac{abc}{\sqrt{(a+b+c)(a+b-c)(b+c-a)(c+a-b)}}$$

where the distances between two of the three points were a, b, and c [13].

Radiographic analysis

All of the radiological assessments were performed using full-length weight-bearing AP radiographs. On taking full-length weight-bearing radiographs, each lower limb was rotated so that the knee pointed anteriorly [21]. No attempt was made to fluoroscopically control the films to avoid excessive radiation exposure.

A point was marked on each radiograph in the center of the intramedullary canal at the proximal and distal third of the femur. A line connecting these two points was defined as the femoral anatomic axis [15]. The tibial anatomic axis was found in the same manner as above. Anatomical tibiofemoral angle was determined by intersecting the femoral anatomic axis with the tibial anatomic axis [18] (Fig. 3). The lateral angle between a line tangent to both distal femoral condyles and the femoral anatomic axis or the femoral mechanical axis was defined as the femoral joint angle [17], and the hip-condylar angle, respectively (Fig. 3). The lateral angle between the tibial anatomic axis and a line parallel to the proximal articular surface was defined as the tibial joint

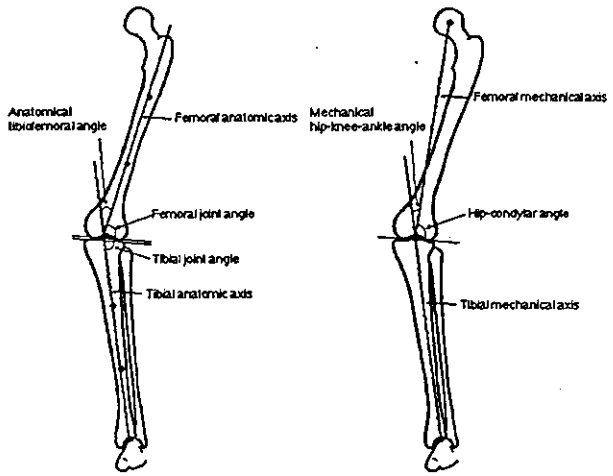

Fig. 3. The femoral anatomic axis passed two points marked in the center of the intramedullary canal of the femur, and the tibial anatomic axis passed two points marked in that of the tibia (Left). The anatomical tibiofemoral angle was created by intersecting the femoral and tibial anatomic axes. The femoral joint angle was the lateral angle between the femoral anatomic axis and a line tangent to both distal femoral condyles. The tibial joint angle was the lateral angle between the tibial anatomic axis and a line parallel to the proximal articular surface. The mechanical hip–knee–ankle angle was created by intersecting the femoral and tibial mechanical axes (Right). The femoral joint angle was the lateral angle between the femoral mechanical axis and a line tangent to both distal femoral condyles.

angle [17] (Fig. 3). The angle between the femoral mechanical axis (a line connecting hip center and knee center) and the tibial mechanical axis (a line connecting knee center and ankle center) was defined as the mechanical, hip–knee–ankle angle [6]. These radiographic parameters were compared among the normal, varus and valgus knees.

Statistical analysis was carried out using a data analysis system (StatView 5.0, Abacus Concepts, Inc., Berkeley, CA). The mean and standard deviations of all measurements were calculated. One factor analysis of variance (ANOVA) and Fisher's PLSD as the post-hoc analysis were used. P values of less than 0.05 were considered to be statistically significant.

Results

The posterior condylar tangent showed 6.4° of internal rotation in the normal knees and 6.1° in the varus knees when the angle to the transepicondylar axis was measured (Table 2, Fig. 4). However, the posterior condylar axis in the valgus knees showed 11.5° of internal rotation (Fig. 5), which was significantly larger than that in the normal and varus knees ($p < 0.0001$). The posterior condylar axis showed 6.3° of internal

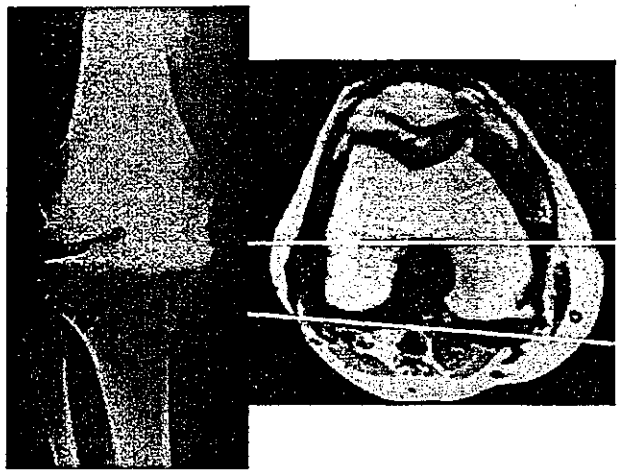

Fig. 4. Standing AP radiograph of the varus knee (Left). Magnetic resonance image of the axial view of the distal femur in the varus knee (Right). The transepicondylar axis was externally rotated 6° from the posterior condylar tangent.

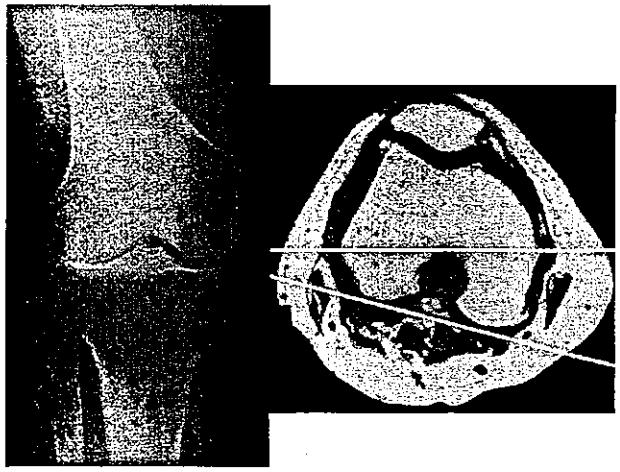

Fig. 5. Standing AP radiograph of the valgus knee (Left). Magnetic resonance image of the axial view of the distal femur in the varus knee (Right). The posterior part of the lateral condyle was relatively small compared to that of the medial condyle, and the transepicondylar axis was externally rotated 11° from the posterior condylar tangent.

Table 2
Magnetic resonance imaging analysis (axial view)

Parameter	Normal knees	Varus knees	Valgus knees
Angle between transepicondylar axis and posterior condylar tangent	6.4 ± 1.8 (3.5–10.6)	6.1 ± 1.8 (0.3–10.7)	11.5* ± 2.1 (8.1–16.9)
Angle between a line perpendicular to the anteroposterior axis and posterior condylar tangent	6.3 ± 12.4 (0.0–10.0)	6.6 ± 2.5 (3.0–12.0)	8.6* ± 2.7 (3.0–13.5)
Angle between anteroposterior axis and transepicondylar axis	90.1 ± 3.2 (84.6–100.6)	89.5 ± 2.8 (82.7–94.6)	92.9* ± 2.6 (87.0–98.0)

*Significantly different from normal knees and varus knees ($p < 0.05$).

Table 3
AP dimension of the femoral condyle

Parameter		Normal knees	Varus knees	Valgus knees
Anterior	Medial condyle	30.6 ± 3.0 (24.8–36.9)	32.4* ± 2.0 (27.9–34.8)	31.9 ± 2.1 (28.7–37.6)
	Lateral condyle	37.1 ± 4.4 (30.3–44.9)	38.3 ± 2.9 (32.7–41.9)	39.5 ± 2.5 (35.2–45.0)
Posterior	Medial condyle	29.2 ± 2.4 (25.6–34.1)	29.6 ± 2.7 (25.6–34.3)	29.9 ± 2.5 (21.6–35.4)
	Lateral condyle	24.1 ± 2.4 (20.5–30.2)	24.7 ± 2.6 (21.6–31.4)	21.9** ± 2.6 (15.6–26.9)

*Significantly different from normal knees ($p < 0.05$).
**Significantly different from normal knees and varus knees ($p < 0.05$).

Table 4
Magnetic resonance imaging analysis (sagittal view)

	Normal knee	Varus knees	Valgus knees
Medial condyle	20.3 ± 3.4 (16.1–28.0)	21.2 ± 2.1 (18.0–24.5)	21.1 ± 2.0 (17.8–24.1)
Lateral condyle	19.0 ± 3.0 (14.7–25.0)	20.8 ± 2.1 (17.5–30.0)	21.1* ± 2.1 (18.4–25.5)

*Significantly different from normal knees ($p < 0.05$).

rotation in the normal knees, 6.6° in the varus knees, and 8.6° in the valgus knees when the angle to the line perpendicular to the AP axis was measured (Table 2). The angle in the valgus knee was significantly larger than that in the normal ($p = 0.0006$) and varus knees ($p = 0.0023$). The AP axis was approximately perpendicular to the transepicondylar axis in normal and varus knees, but the AP axis was slightly internally rotated relative to the transepicondylar axis in valgus knees (Table 2).

In the measurement of the AP dimension of the anterior part of the lateral condyle, no significant difference was detected between normal, varus, and valgus knees, however the AP dimension of the medial condyle in the varus knee was significantly larger ($p = 0.0460$) than in the normal knees (Table 3). No significant difference was found in the AP dimension of the posterior part of the medial condyle between normal, varus, and valgus knees; however, the AP dimension of the lateral condyle in the valgus knee was significantly smaller than in the normal ($p = 0.0044$) and valgus knees ($p = 0.0014$) (Table 3).

Measurement of the radius of the posterior part of the medial femoral condyle did not reveal any significant differences between normal, varus, and valgus knees. The radius of the posterior part of the lateral femoral condyle in valgus knees was significantly larger ($p = 0.0384$) than the value in normal knees (Table 4, Fig. 6).

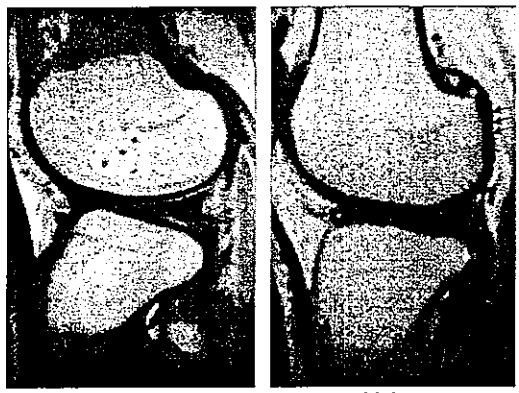

Fig. 6. Magnetic resonance image shows a sagittal view of the distal femur in a normal knee (Left). Magnetic resonance image shows a sagittal view of the distal femur in a valgus knee (Right). The posterior part of the lateral condyle is flat in shape.

In radiographic analysis, the anatomical tibiofemoral angle was 3.6° valgus in the normal knees, 5.0° varus in the varus knees, and 13.3° valgus in the valgus knees (Table 5). The patients with the varus and the valgus

Table 5
Radiographic analysis

Parameter	Normal knees	Varus knees	Valgus knees
Anatomical tibiofemoral angle	3.6 ± 2.2 (0.4–8.0)	−5.0** ± 7.0 (−30.0–6.0)	13.3* ± 4.9 (4.2–25.8)
Mechanical hip–knee–ankle angle	−1.4 ± 2.4 (−6.0 to −1.0)	−14.2** ± 5.3 (−23.0 to −6.0)	9.1* ± 6.3 (−0.7–20.8)
Femoral joint angle	83.3 ± 1.5 (80.3–85.9)	83.8 ± 2.0 (78.9–88.9)	80.7* ± 1.9 (76.7–85.0)
Hip–condylar angle	88.3 ± 2.3 (84.3–91.2)	90.4 ± 3.2 (84.9–97.0)	85.1* ± 2.3 (81.5–90.0)
Tibial joint angle	93.0 ± 1.3 (90.3–96.1)	94.3** ± 2.3 (90.1–98.6)	91.0* ± 3.2 (84.8–99.2)

*Significantly different from normal knees and varus knees ($p < 0.05$).
**Significantly different from normal knees and valgus knees ($p < 0.05$).

knees had 8.6° of varus and 9.6° of valgus deformity, respectively, compared to those with the normal knees. The mechanical, hip–knee–ankle angle was 1.4° varus in the normal knees, 14.2° varus in the varus knees, and 9.1° valgus in the valgus knees (Table 5). The femoral joint angle and the hip-condylar angle in the valgus knees was significantly smaller ($p < 0.001$) than those in the normal and varus knees (Table 5). The tibial joint angle in the valgus knees was significantly smaller than that in the normal knees ($p = 0.002$) and varus knees ($p < 0.001$), and the angle in the varus knees was significantly larger ($p = 0.032$) than that in the normal knees (Table 5).

Discussion

Proper rotational alignment of the component is one of the most important factors for successful total knee arthroplasty [1,4,14]. Previous studies recommended that the femoral component should be inserted parallel to the transepicondylar axis [5,8] or to the AP axis [3]. However, accurate detection of both the medial and lateral epicondyle is sometimes difficult [3,11], as is finding the AP axis, because of trochlear wear or intercondylar osteophytes in arthritic knees [19]. The posterior condyles can be more easily identified intraoperatively, therefore some bone cutting guide systems are designed to align the femoral component in 3–5° of external rotation from the posterior condyles. These systems align the femoral component parallel to the transepicondylar axis with a small amount of deviation, because the previous anatomical studies have shown that the transepicondylar axis is externally rotated from the posterior condylar tangent in 3–6° [2,8,9,13,22]. These anatomical studies are mainly focused on the normal or varus knees, but detailed measurement of surface geometry has not been available in valgus knees probably because valgus knee deformity is relatively rare knee condition. Griffin, et al. [8] measured the angle between the surgical epicondylar axis and the posterior condylar tangent intraoperatively and reported an average angle of 3.3° for varus knees and 5.4° for valgus knees. In that study, valgus knees were defined as knees with anatomical tibiofemoral angles greater than 7°, but the average and range of the anatomical tibiofemoral angles of the valgus knee group are unknown, and questions remain on the accuracy of intraoperative measurement. Akagi, et al. [2] measured the angle between the clinical epicondylar axis and the posterior condylar tangent as 9.1° for valgus knees and 6.4° for normal knees. However, the valgus knee group included both rheumatoid and osteoarthritis, and computed tomography evaluated the bony boundaries but not the articular boundaries of the femoral condyles. Therefore, femoral condyle geometry has not been fully evaluated in osteoarthritic knees with valgus deformity.

The results of our study showed that the posterior condylar tangent was internally rotated against the transepicondylar axis approximately 6° in both the normal and varus knees and 11.5° in the valgus knees. In performing total knee arthroplasty for a valgus knee, 3° of external rotation from the posterior condyles results in internal rotation of the femoral component relative to the transepicondylar axis by 8.5°. This amount of malrotation of the femoral component could cause patellofemoral joint complications [1,4,14]. The surgeon should take deformity of the lateral condyle into account, and the angle between the transepicondylar axis and the posterior condylar tangent should be measured using MRI (or computed tomography) before surgery. With the measured external rotational angle, easily detectable posterior condyles can be used as a reliable rotational landmark in addition to palpation of the epicondyles.

In the valgus knees, the AP dimension of the posterior part of the lateral condyle was significantly smaller than in the normal and varus knees, but the anterior part of the lateral condyle did not show a significant difference. Also in the valgus knees, we can conclude that the posterior part of the lateral condyle is relatively flat in shape based on the findings that the radius of the posterior arc of the lateral femoral condyle was significantly larger than in the normal knees. These findings suggest that the posterior part of the lateral condyle in the valgus knees is distorted, but there is no hypoplasia in the posterior part of the medial condyle in the varus knees. Therefore, distorted posterior condyles are the main mechanism causing the posterior condylar tangent to be more internally rotated in the valgus knees than in the normal and varus knees, relative to the transepicondylar axis. The AP dimension of the anterior part of the medial condyle in the varus knees was larger than in the normal knees, probably due to osteoarthritic changes of the anterior condyles.

The results of this study also showed that the AP axis was approximately perpendicular to the transepicondylar axis in normal and varus knees, but slightly internally rotated in valgus knees. We cannot conclude which landmark should be used in valgus knees from our results; however, these results suggest that the AP axis measurements might deviate due to distorted arthritic articular geometry.

The results of the coronal plane (radiographic) analysis showed that the femoral joint angle in the valgus knees was significantly smaller than that in the varus and the normal knees, but no significant difference was detected between the varus knees and the normal knees. These results suggests that hypoplasia was not present in the distal part of the medial condyle in the varus knees, but the distal part of the lateral condyle in the valgus knees was distorted, as well as the posterior part of the lateral condyle, although the difference detected was

more distinct in the posterior part. It was unclear whether the distorted lateral condyle in the valgus knees was the factor contributing to osteoarthritis of the lateral compartment of the knee or was a result of the valgus deformity. A significant difference in the distal femur geometry was detected between the normal and valgus knees, but not detected between the normal and varus knees, even though patients with the varus knees had the same degree of knee deformity as those with the valgus knees in anatomical tibiofemoral angle. Therefore, we could say that osseous abnormality of the femur contributed to the knee deformity more predominantly in valgus knees than in varus knees. From the findings of this study, however, we are unable to conclude that the distorted lateral femoral condyle caused osteoarthritis of the lateral compartment.

The tibial joint angle in the normal knees was significantly smaller than that in the varus knees and significantly larger than that in the valgus knees, suggesting that osseous abnormality of the tibia exists in both the varus and valgus knees and that the tibial deformity is the contributing factor to the overall malalignment of the leg. Both the varus and valgus knees had lowered tibial plateau in the affected compartment compared to the normal knees, suggesting that osseous abnormality of the tibia was possibly caused by degenerative changes of osteoarthritis rather than by developmental abnormality.

The current study has some limitation. Better matching of the groups in terms of gender and age may have strengthened the study. It was difficult, however, to do this because valgus knee deformity is a relatively rare knee condition. Many studies have shown that no marked difference is present in femoral condyle geometry between male and female [8,9,19,23]. Therefore, we believe the heavy preponderance of females in our valgus knee group did not significantly affect our results. In addition, all of the anatomic specimens in the current study were Japanese; therefore, these findings may not apply to other racial groups.

In summary, radiographic and MRI analysis showed that hypoplasia of the lateral condyle existed in the valgus knees, but not in the medial condyle in the varus knee. In total knee arthroplasty for valgus knee, the extent of hypoplasia of the lateral condyle should be evaluated preoperatively to achieve the correct rotational alignment.

References

[1] Akagi M, Matsusue Y, Mata T, et al. Effect of rotational alignment on patellar tracking in total knee arthroplasty. Clin Orthop 1999;366:155–63.

[2] Akagi M, Yamashita E, Nakagawa T, et al. Relationship between frontal knee alignment and reference axes in the distal femur. Clin Orthop 2001;388:147–56.

[3] Arima J, Whiteside LA, McCarthy DS, White SE. Femoral rotational alignment, based on the anteroposterior axis, in total knee arthroplasty in a valgus knee. J Bone Joint Surg [Am] 1995;77:1331–4.

[4] Berger RA, Crossett LS, Jacobs JJ, Rubash HE. Malrotation causing patellofemoral complications after total knee arthroplasty. Clin Orthop 1998;356:144–53.

[5] Berger RA, Rubash HE, Seel MJ, et al. Determining the rotational alignment of the femoral component in total knee arthroplasty using the epicondylar axis. Clin Orthop 1993;286:40–7.

[6] Cooke D, Scudamore A, Li J, et al. Axial lower-limb alignment: comparison of knee geometry in normal volunteers and osteoarthritis patients. Osteoarthr Cartilage 1997;5:39–47.

[7] Elias SG, Freeman MAR, Gokcay EI. A correlative study of the geometry and anatomy of the distal femur. Clin Orthop 1990;260:98–103.

[8] Griffin FM, Insall JN, Scuderi GR. The posterior condylar angle in osteoarthritic knees. J Arthroplasty 1988;12:812–5.

[9] Griffin FM, Math K, Scuderi GR, et al. Anatomy of the epicondyles of the distal femur. MRI analysis of normal knees. J Arthroplasty 2000;15:354–9.

[10] Hollister AM, Jatana S, Singh AK, et al. The axes of rotation of the knee. Clin Orthop 1993;290:259–68.

[11] Katz MA, Beck TD, Silber JS, et al. Determining femoral rotational alignment in total knee arthroplasty: reliability of techniques. J Arthroplasty 2001;16:301–5.

[12] Kurosawa H, Walker PS, Garg A, Hunter T. Geometry and motion of the knee for implant and orthotic design. J Biomech 1985;18:487–99.

[13] Matsuda S, Matsuda H, Miyagi T, et al. Femoral condyle geometry in the normal and varus knee. Clin Orthop 1998;349:183–8.

[14] Matsuda S, Miura H, Nagamine R, et al. Effect of the femoral and tibial component position on patellar tracking following total knee arthroplasty. 10-year follow-up of Miller Galante I knees. Am J Knee Surg 2001;14:152–6.

[15] Moreland JR, Bassett LW, Hanker GJ. Radiographic analysis of the axial alignment of the lower extremity. J Bone Joint Surg [Br] 1987;69:745–9.

[16] Murray PB, Rand JA. Symptomatic valgus knee: the surgical options. J Am Acad Orthop 1993;1:1–9.

[17] Nagamine R, Miura H, Bravo CV, et al. Anatomic variations should be considered in total knee arthroplasty. J Orthop Sci 2000;5:232–7.

[18] Petersen TL, Engh GA. Radiographic assessment of knee alignment after total knee arthroplasty. J Arthroplasty 1988;3:67–72.

[19] Poilvache PL, Insall JN, Scuderi GR, Font-Rodriguez DE. Rotational landmarks and sizing of the distal femur in total knee arthroplasty. Clin Orthop 1996;331:35–46.

[20] Phillips MJ, Krackow KA. Distal femoral varus osteotomy. Indications and surgical technique. Inst Course Lec 1999;48:125–9.

[21] Siu D, Cooke TDV, Brokenhoven LD, et al. A standardized technique for lower limb radiography: practice, applications, and error analysis. Invest Radiol 1991;26:71–7.

[22] Yoshino N, Takai S, Ohtsuki Y, Hirasawa Y. Computed tomography measurement of the surgical and clinical transepicondylar axis of the distal femur in osteoarthritic knees. J Arthroplasty 2001;16:493–7.

[23] Yoshioka Y, Siu D, Cooke TDV. The anatomy and functional axes of the femur. J Bone Joint Surg [Am] 1987;69:873–80.

Available online at www.sciencedirect.com

SCIENCE DIRECT

Journal of Controlled Release 100 (2004) 317–330

journal of controlled release

www.elsevier.com/locate/jconrel

Review

Novel strategic therapeutic approaches for prevention of local recurrence of pancreatic cancer after resection: trans-tissue, sustained local drug-delivery systems

Tatsuya Manabe[a,b], Hidenobu Okino[a,b], Ryo Maeyama[a,b], Kazuhiro Mizumoto[b], Eishi Nagai[b], Masao Tanaka[b], Takehisa Matsuda[a,*]

[a]*Division of Biomedical Engineering, Graduate School of Medicine, Kyushu University, 3-1-1 Maidashi, Fukuoka 812-8582, Japan*
[b]*Division of Surgery and Oncology, Graduate School of Medicine, Kyushu University, 3-1-1 Maidashi, Higashi-ku, Fukuoka 812-8582, Japan*

Received 27 May 2004; accepted 15 September 2004
Available online 19 October 2004

Abstract

Local recurrence and hepatic metastasis are still the major causes of death of patients who have undergone resection for pancreatic cancer. To decrease the incidence of local recurrence, we have proposed and devised several trans-tissue and local delivery systems, all of which could be applied immediately after surgery at the resected sites: (1) System I: a drug-loaded photocured gelatinous tissue-adhesive gel (bioactive substance reservoir) that enables the sustained release of a drug, protein, or gene-encoding adenovirus, (2) System II: an anti-cytokine antibody-fixed photocured gelatinous, tissue-adhesive gel (cytokine barrier) that prevents cytokine permeation into the resected tissue, (3) System III: a gene-modified cell sheet that enables the sustained release of a very costly protein produced by gene-transduced cells and (4) System IV: a percutaneous drug-delivery device that enables continuous drug infusion and easy removal from the body. This review article is a summary of our several years of efforts and attempts, which are composed of integrated disciplines including active biomaterials and genetic- and tissue-engineerings, to overcome the recurrence of pancreatic cancer. Here, we outline our proposed strategies and therapeutic devices/materials and discuss their potential therapeutic effectiveness, promises and challenges in the clinical settings.

Keywords: Local drug delivery; Pancreatic cancer; Local recurrence; Cytostasic therapy; Cytocidal therapy

* Corresponding author. Tel.: +81 92 642 6211; fax: +81 92 642 6212.
E-mail address: matsuda@med.kyushu-u.ac.jp (T. Matsuda).

0168-3659/$ - see front matter © 2004 Elsevier B.V. All rights reserved.
doi:10.1016/j.jconrel.2004.09.007